

On mm-Wave Multipath Clustering and Channel Modeling

Carl Gustafson, Katsuyuki Haneda, *Member, IEEE*, Shurjeel Wyne, *Senior Member, IEEE*, and Fredrik Tufvesson

Abstract—Efficient and realistic mm-wave channel models are of vital importance for the development of novel mm-wave wireless technologies. Though many of the current 60 GHz channel models are based on the useful concept of multipath clusters, only a limited number of 60 GHz channel measurements have been reported in the literature for this purpose. Therefore, there is still a need for further measurement based analyses of multipath clustering in the 60 GHz band. This paper presents clustering results for a double-directional 60 GHz MIMO channel model. Based on these results, we derive a model which is validated with measured data. Statistical cluster parameters are evaluated and compared with existing channel models. It is shown that the cluster angular characteristics are closely related to the room geometry and environment, making it infeasible to model the delay and angular domains independently. We also show that when using ray tracing to model the channel, it is insufficient to only consider walls, ceiling, floor and tables; finer structures such as ceiling lamps, chairs and bookshelves need to be taken into account as well.

Index Terms—60 GHz WLAN, channel modeling, IEEE 802.11ad, IEEE 802.15.3c, millimeter wave propagation.

I. INTRODUCTION

AS the requirements for efficient and reliable wireless communications with high throughput are ever-increasing, novel wireless techniques have to be considered, and the available radio spectrum has to be used efficiently in order to overcome spectrum shortage. Due to the large bandwidth of at least 5 GHz available worldwide [1], the 60 GHz band is a promising candidate for short-range wireless systems that require very high data rates. Efforts have already been made regarding standardization by the IEEE 802.15.3c [2] and IEEE 802.11ad [3] working groups, and some commercial products are already available on the market.

The propagation characteristics in the 60 GHz band are quite different from those in the lower frequency bands commonly used today for cellular communication. Assuming identical

transmit powers and antenna gains, the received power at 60 GHz is smaller than that at lower frequencies due to a smaller receive antenna aperture at 60 GHz. Furthermore, since the dimensions of typical shadowing objects are large in relation to the wavelength at 60 GHz, sharp shadow zones are formed, making diffraction an insignificant propagation mechanism [4]. Also, due to the high penetration loss of most materials at 60 GHz, multipath components propagating through walls or other objects typically have low power. Due to these propagation characteristics, highly directional antennas or adaptive beam-forming techniques are required in order to establish a reliable 60 GHz communication link [5].

As the potential benefits of systems operating in the 60 GHz band are directly related to the propagation environment characteristics, realistic and reliable channel models are of vital importance for the design and development of novel 60 GHz technologies. Furthermore, as beam forming techniques are vital for many types of mm-wave communications, the channel should ideally be modeled using a MIMO model that takes the angular characteristics of the channel into account.

The IEEE802.11ad channel model is a MIMO model based on a mixture of ray tracing and measurement-based statistical modeling techniques [6]. It is a cluster-based spatio-temporal channel model that supports several different environments. The measurements for the IEEE802.11ad model were conducted using highly directional antennas that were steered in different directions in order to evaluate and model the cluster parameters of 60 GHz channels.

Several recent studies are directly related to the IEEE802.11ad model and include theoretical investigations regarding capacity [7], spatial diversity techniques [8] and beamforming performance [9], as well as an extended model for human blockage in 60 GHz channels [10].

In this paper, we present measurement-based results for a double-directional 60 GHz MIMO channel model in a conference room environment. Statistical cluster parameters are evaluated and compared with existing 60 GHz channel models. The novel aspect of our proposed channel model is the method by which it models the spatio-temporal properties of the clusters. We provide two different ways of modeling the cluster spatio-temporal properties; one being stochastic and the other a semi-deterministic approach that is based on ray-tracing. Most of the current 60 GHz directional analyses rely on measurements using highly directional antennas that are mechanically steered [11] and sometimes also include ray tracing results [6]. The results in this paper are based on measurements using the virtual antenna array technique. The double-directional estimates for the multipath components (MPCs) were obtained using the

Manuscript received July 02, 2013; revised October 21, 2013; accepted November 29, 2013. Date of publication December 23, 2013; date of current version February 27, 2014.

C. Gustafson and F. Tufvesson are with the Department of Electrical and Information Technology, Lund University, Sweden (e-mail: carl.gustafson@eit.lth.se).

K. Haneda is with the Department of Radio Science and Engineering, Aalto University, School of Science and Technology, Finland.

S. Wyne is with the Department of Electrical Engineering, COMSATS Institute of Information Technology, Islamabad, Pakistan.

Color versions of one or more of the figures in this paper are available online at <http://ieeexplore.ieee.org>.

Digital Object Identifier 10.1109/TAP.2013.2295836

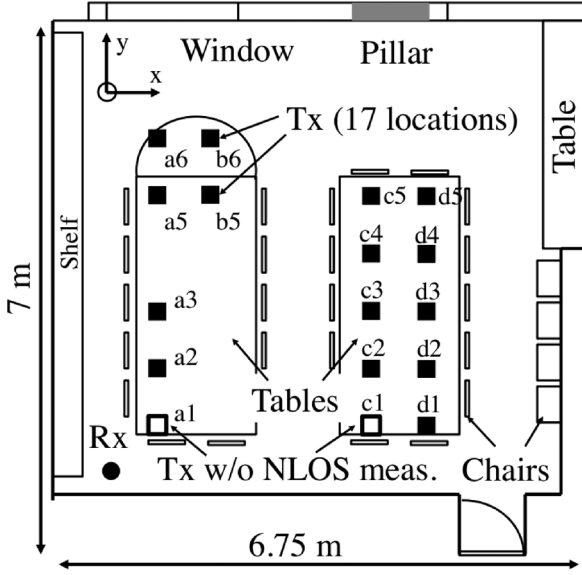


Fig. 1. Floorplan of the measured conference room.

SAGE algorithm. This technique can potentially offer an improved resolution of the MPC parameters compared with techniques based on mechanically steered high-gain antennas [6]. The clustering results were then obtained using an automated clustering algorithm.

II. 60 GHz RADIO CHANNEL AND ANTENNA MEASUREMENTS

A. Measurement Environment

This work is based on results from a 60 GHz radio channel measurement campaign performed in a conference room with a volume of $6.8 \times 7.0 \times 2.5 \text{ m}^3$. The IEEE802.11ad working group has performed measurements in smaller conference rooms with volumes of approximately $3 \times 4.5 \times 3 \text{ m}^3$ [12] and in a slightly larger conference room with a width and length of 6.3 m and 4.3 m [13]. During our measurements, the Rx array was placed at a fixed position in one of the corners of the room whereas the Tx array was placed at one of 17 predefined positions on either of the two tables in the room. As indicated by Fig. 1, 17 different line-of-sight (LOS) measurements were performed at these positions as well as 15 additional obstructed-line-of-sight (OLOS) measurements. In the OLOS scenarios, a laptop computer screen was used to block the direct path between the Tx and the Rx. Further details about the measurements can be found in [14].

B. Measurement Equipment and Setup

The 60 GHz radio channel was measured using a vector network analyzer based system [15]. 2-D electromechanical positioners were used to move the Tx and Rx antennas in the horizontal and vertical planes, respectively. A commercial biconical antenna, Flann Microwave MD249, with an omnidirectional pattern in azimuth was used at the Tx side, and the Tx virtual array was a horizontal uniform rectangular array with 7×7 elements. The Rx antenna was an open waveguide, vertically polarized and oriented such that the waveguide opening was directed towards the opposite corner of the room

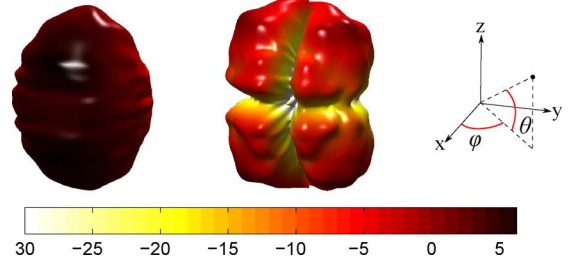


Fig. 2. Co-polarized (left) and cross-polarized (right) Rx antenna gain in dBi of the open waveguide at 62 GHz.

compared to where the Rx array was situated. The Rx virtual array was a vertical uniform rectangular array with 7×7 elements. All measurements were performed with the antennas in a vertical-to-vertical (V-V) polarization orientation. The interelement spacing was 2 mm in both arrays. Back-to-back measurements were performed in order to remove the influence of the coaxial cables, mixers, and feeding waveguides.

C. Antenna Measurements

The co- and cross-polarized antenna gains of the Tx- and Rx antenna were first measured using a setup based on a vector network analyzer (VNA) and electromechanical positioners. A standard gain horn antenna with known gain and high cross-polarization discrimination ratio was used as the reference antenna. Electromagnetic absorbers were used to cover equipment in the close vicinity of the antenna, such as the VNA, positioners and tables. Also, since the measurements were performed in a large open area in a room, the data will also include effects due to possible multipath propagation within the room. A simple time-domain gating technique was employed to filter the measured data and remove parts of the impulse response with longer delays. The frequency range in the measurement was 60–64 GHz, yielding a time resolution of 0.25 ns. The gain transfer method [16] was then employed to calculate the antenna gain. Due to the small wavelength and considering the alignment accuracy of the measurement setup, it was not possible to extract the phase responses of the antennas precisely. Fig. 2 shows the co- and cross-polarized antenna gains of the Rx antenna at 62 GHz. The cross-polarized antenna gain of the biconical Tx antenna (not shown) is low in all directions, whereas the cross-polarized antenna gain of the open waveguide is fairly high in certain directions.

Using the measured co- and cross-polarized data, it was possible to estimate the cross-polarization discrimination ratio (XPD) of the antennas as

$$\text{XPD}(\phi, \theta)_{\text{dB}} = G_{\text{co}}(\phi, \theta)_{\text{dB}} - G_{\text{cross}}(\phi, \theta)_{\text{dB}}. \quad (1)$$

In other words, we define the antenna XPD to be the difference between the co-polarized and cross-polarized antenna gain in a certain angular direction. This is of importance since the measurements were performed only with V-V polarization, which means that it is not possible to employ a full polarimetric estimation of the complex amplitudes in SAGE. Instead, only the complex gain of the V-V component is estimated. This means that the SAGE algorithm only produces accurate results

for MPCs in directions where the XPDs of the Tx and Rx antennas are large [17]. In total, less than 5% of the total number of MPCs in all scenarios were located in directions where the XPD was lower than 20 dB.

III. MULTIPATH ESTIMATION AND CLUSTERING

A. SAGE Algorithm

The measured transfer functions are assumed to be correctly described by a finite number of plane waves, i.e., multipath components (MPCs). Each MPC is described by its complex amplitude, delay, direction of departure (DOD) and direction of arrival (DOA). In order to estimate these MPC parameters, the SAGE algorithm is used. A double-directional analysis using SAGE based on the same measurements was previously presented in [18], and the reader is referred to that paper for details regarding the signal model for the analysis. This work improves the SAGE estimates of [18] by employing a more detailed model for the gain patterns of the antennas used in the measurements. By taking the gain of the antennas into account, the estimated results describe the propagation channel.

The SAGE analysis was performed over an observation bandwidth of 200 MHz centered at 62 GHz with 26 equi-spaced frequency samples. The estimated MPCs can be used to model the 2 GHz band from 61–63 GHz because the multipath parameters do not change drastically over this frequency band. This assertion is justified by the fact that neither the power angular profiles [19], nor the SAGE estimates change drastically when evaluated at center frequencies of 61, 62 and 63 GHz.

B. Clustering Method

In this paper, a cluster is defined as a group of multipath components having similar delays and directions of departure and arrival. The estimated MPCs are grouped into clusters using the K-power-means algorithm wherein the multipath component distance is used as a distance metric in parameter space [20]. For the validation of the number of clusters, the Kim-Parks index [21] was utilized. The Kim-Parks index, KP , can be considered as a normalized version of the Davies-Bouldin index. It is calculated using an over- and under-partition measure function, v_o and v_u , that are normalized with respect to the minimum and maximum number of clusters, C_{\min} and C_{\max}

$$KP(C) = v_o(C) + v_u(C). \quad (2)$$

The optimal number of clusters, C_{opt} , for a certain scenario is then given by

$$C_{opt} = \underset{C}{\operatorname{argmin}} \{KP(C)\}, \quad C_{\min} \leq C \leq C_{\max}. \quad (3)$$

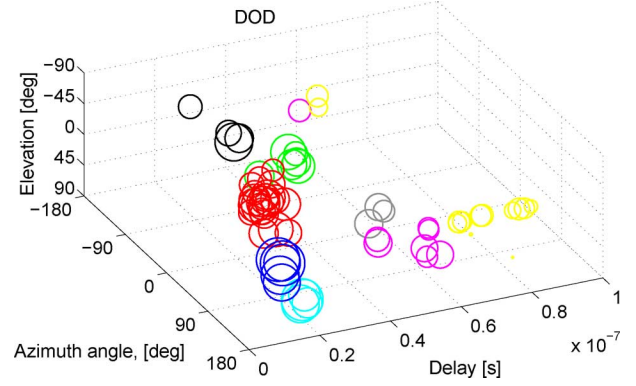


Fig. 3. Typical clustering result for the direction of departure.

In practice, the largest number of clusters is set to be a number that is large enough to make sure that the correct number of clusters is identified. For a more detailed description of the Kim-Parks index, the reader is referred to [21]. The Kim-Parks index was chosen over the combined validation scheme as it produced consistent results that agreed better with the number of cluster identified based on a visual inspection. When using the Kim-Parks index, the number of identified clusters ranged from 6 to 12 in the LOS scenario and 8 to 12 in the OLOS scenario. Fig. 3 show typical clustering results for the direction of departure. Similar results were obtained for the direction of arrival. Each circle represents an MPC and the colors indicate identified clusters and the radius of each circle is proportional to the power of each MPC. In order to get more consistent results in the LOS and OLOS scenarios, the clustering in the LOS scenarios are performed without including the LOS component. That way, the power levels are similar in both scenarios. It is possible to exclude the LOS component from the clustering since this component can be treated deterministically. The clustering results for the LOS and OLOS scenarios are very similar. The main differences between the LOS and OLOS scenarios are

- 1) A strong LOS component present in the LOS scenario.
- 2) A number of components are present in the OLOS scenario that are diffracted around the computer screen.

IV. SURVEY OF 60 GHz CHANNEL MODELS

A. Extended Saleh-Valenzuela Model

Based on the clustering results, a number of statistical 60 GHz channel model parameters can be derived. One of the most widely used channel models based on clusters is the extended Saleh-Valenzuela model, where the impulse response, h , is given by (4) at the bottom of the page. Here, $\beta_{k,l}$ is the complex amplitude of the k th ray (i.e., MPC) in the l th cluster and T_l , Ω_l and Ψ_l are the delay, DOA and DOD of the l th

$$h(t, \Theta_{rx}, \Theta_{tx}) = \sum_{l=0}^L \sum_{k=0}^{K_l} \beta_{k,l} e^{j\chi_{k,l} t} \delta(t - T_l - \tau_{k,l}) \delta(\Theta_{rx} - \Omega_l - \omega_{k,l}) \delta(\Theta_{tx} - \Psi_l - \psi_{k,l}) \quad (4)$$

cluster, respectively. Similarly $\tau_{k,l}$, $\omega_{k,l}$ and $\psi_{k,l}$ are the delay, DOA and DOD of the k th ray in the l th cluster, respectively. Finally, $\delta(\cdot)$ is the Dirac delta function and the phase of each ray, $\chi_{k,l}$, is assumed to be described by statistically independent random variables uniformly distributed over $[0, 2\pi)$. The mean power of the k th ray in the l th cluster is given by

$$\overline{\beta_{k,l}^2} = \overline{\beta(0,0)^2} e^{-T_l/\Gamma} e^{-\tau_{kl}/\gamma} \quad (5)$$

where Γ and γ are the cluster and ray decay constants, respectively, and $\overline{\beta(0,0)^2}$ is the average power of the first ray in the first cluster [22].

If the delay and angular domains can be modeled independently, the cluster and ray arrival time distributions may be described by two Poisson processes. Under this assumption, the cluster and ray interarrival times are typically described by two independent exponential probability density functions. The cluster arrival time for each cluster is thus described by an exponentially distributed random variable that is conditioned on the arrival time of the previous cluster, i.e.,

$$p(T_l|T_{l-1}) = \Lambda e^{-\Lambda(T_l - T_{l-1})}, \quad l > 0. \quad (6)$$

Here, Λ is the cluster arrival rate. Similarly for the ray arrival times, we have

$$p(\tau_{k,l}|\tau_{k-1,l}) = \lambda e^{-\lambda(\tau_{k,l} - \tau_{k-1,l})}, \quad l > 0 \quad (7)$$

where λ is the ray arrival rate.

The extended S-V model relies on the assumption that the delay and angular domains can be modeled independently. As will be shown later, this assumption might not be valid for 60 GHz channels. Instead, it is necessary to either jointly model the angular and delay domains using a joint angular-delay distribution [23], or to use a deterministic approach based on ray tracing, which is done in the IEEE 802.11ad channel model [6]. This will be discussed further in Section VI.

B. IEEE 802.15.3c Channel Model

In the IEEE802.15.3c channel model, the extended S-V model of (4) is used with the addition of a LOS component that is derived deterministically. It is a SIMO model that only models the DOA. The cluster DOA is modeled using a uniform distribution in the range $[0, 2\pi)$. Cluster arrival times are modeled using a certain cluster arrival rate as in (6) [24].

C. IEEE 802.11ad Channel Model

The IEEE802.11ad channel model is similar to that of the extended S-V model. However, in contrast to the 802.15.3c model, the delay, DOD and DOA for clusters are derived from empirical distributions for different types of first and second order clusters stemming from, e.g., ceiling and wall-ceiling interactions. The gain of the clusters are determined based on propagation and reflection losses, where the reflection losses are modeled using truncated log-normal distributions. The rays within each cluster are modeled using a central ray and a number of pre- and post-cursor rays. The pre- and post-cursor rays are modeled using different arrival times, λ_{pre} and λ_{post} , decay rates, γ_{pre} and γ_{post} , and average ray amplitudes. The pre- and post-cursor

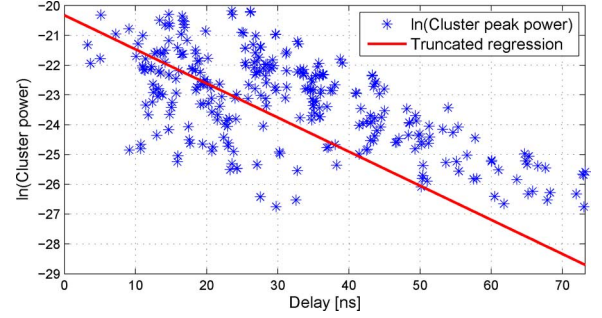


Fig. 4. Cluster peak power as a function of absolute delay and the estimated cluster decay based on a truncated model for the clusters.

rays also have K-factors, K_{pre} and K_{post} , related to the amplitude of the main ray [6].

V. CLUSTERING RESULTS

Cluster-based channel models rely on two sets of parameters, namely inter- and intracluster parameters, describing the clusters and the rays in each cluster, respectively. In this section, results regarding the estimated inter- and intracluster parameters are presented and related to the channel models discussed above.

A. LOS Component

In our model, the Tx-Rx distance is assumed to be known and is used as an input to the model. For the LOS scenarios, the power of the direct wave (the LOS component) is modeled deterministically based on the free space path loss. The delay of the LOS component is determined by the Tx-Rx separation. Furthermore, the location of the Tx and Rx arrays are assumed to be known, so that the DOD and DOA of the LOS component can be determined.

B. Intercluster Parameters

The cluster peak power is taken as the strongest MPC in each cluster. In this paper, we estimate the cluster decay using the cluster power and delay in absolute units, making it possible to estimate the cluster decay without normalizing the clusters with respect to delay and power of the first cluster. This also allows the noise floor to be kept at a constant level for all the different measurements. This way, the effect of clusters that might be located below the noise floor, and might thus have been missed, can be taken into account by modeling the clusters using a truncated normal distribution. Then, the cluster decay constant Γ was estimated based on a likelihood expression for this truncated model [25]. The cluster peak power and the result of the truncated regression is shown in Fig. 4.

As the LOS component already is being modeled deterministically, it was omitted when estimating the cluster decay for the LOS scenario. When estimating the decay constants for the LOS and OLOS scenarios separately, they were both estimated to be $\Gamma = 8.7$ ns. Hence, the cluster decay can be modeled using the same value for both the LOS and OLOS scenarios. Fig. 4 shows the cluster peak power for the LOS and OLOS scenarios combined. The estimated data for the combined data also yielded a value of $\Gamma = 8.7$ ns.

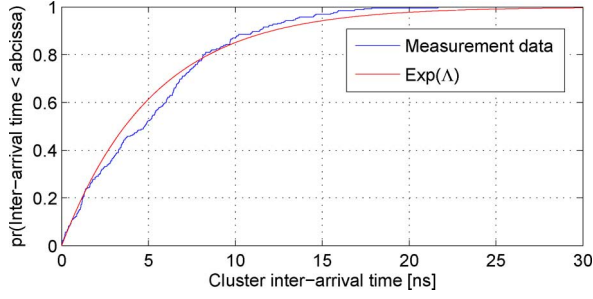


Fig. 5. CDF of the cluster interarrival times and an exponential distribution with a MLE of the parameter Λ .

It was found that the cluster peak power variation around the mean could be appropriately modeled using a log-normal distribution, which corresponds to a normal distribution in the dB-domain. The estimated value for the standard deviation of this normal distribution was found to be the 6.4 dB in both the LOS and OLOS scenarios.

The cluster interarrival times can be described by an exponential distribution. Fig. 5 shows a CDF of the cluster interarrival times and an exponential distribution with an MLE of the parameter Λ . For both the LOS and OLOS scenarios, the estimated cluster arrival rate is $1/\Lambda = 5$ ns.

C. Modeling Cluster Angles and Delays

As shown in Figs. 6 and 7 below, it is not feasible to assume independence between the delay and angular properties of clusters. In the IEEE802.11ad model, this dependence is taken into account by modeling the cluster delays and angles deterministically, based on ray tracing results. In this paper, we consider two different ways of modeling the spatio-temporal properties of clusters; one being stochastic and one being deterministic (i.e., based on ray tracing). These two approaches both have their own strengths and weaknesses, depending on the intended use:

- Ray tracing is site-specific, which could be an advantage when assessing the performance at a specific site. However, when it comes to assessing the overall statistics of 60 GHz MIMO channels, it requires accurate ray tracing results for many different Tx- and Rx-positions, making it ineffective.
- Conversely, a stochastic model can not provide information about a specific room or site, but can effectively reproduce the stochastic properties of 60 GHz channels in a given type of environment.

From now on, these two models are referred to as the ray tracing model and the stochastic model and they are presented in detail below.

1) *Ray Tracing Model*: In the deterministic model, a ray tracing algorithm is used to determine the first and second order reflections, and the corresponding azimuth and elevation angles, as well as delays. In this paper, a simple 3-D image-based ray tracing algorithm is used, where the conference room is modeled as a parallelepiped with the same overall dimensions as the conference room and with tables as the only objects in the room. The conference room geometry is modeled in the same way in the IEEE802.11ad model [6] and has the advantage of being

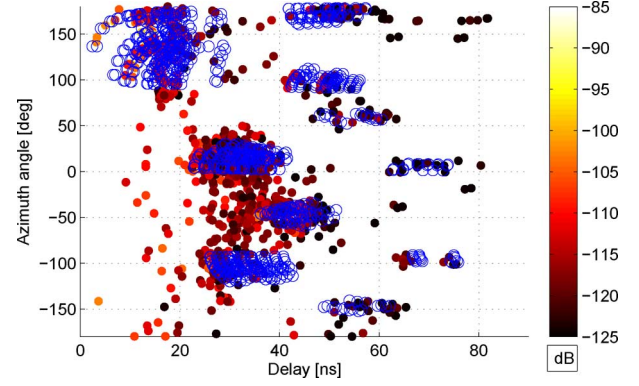


Fig. 6. Delay and azimuth angles of estimated multipath components (dots) and ray-tracing results for first, second and third order reflections (circles).

simple to use for modeling purposes. Fig. 6 compares the delay and azimuth angles of the estimated multipath components with those of a ray-tracing simulations for all LOS scenarios. The elevation angles are not shown here for improved clarity. There is an overall agreement between the ray-tracing and measurement results, but at the same time, a large number of significant MPCs that have been estimated are *not* accurately captured by the ray tracing algorithm. The high resolution estimates of MPC delays and angles were matched with the furniture placement in the room such that it was confirmed that most of these MPCs were interacting with objects such as ceiling lamps, chairs and bookshelves, i.e., objects that are not included in the ray tracing model.

The results from the ray tracing algorithm can not be used directly with the parameters derived for the intracuster parameters, since the ray-tracing results are inconsistent with the cluster definition used in the clustering algorithm. When employing ray tracing, a number of possible reflections are identified, and all of these could be modeled as clusters. However, the intracuster parameters are all based on the results found using the clustering algorithm. In this algorithm, a cluster is defined as a group of MPCs that are close to each other in the spatio-temporal domain, whereas the “clusters” found using ray tracing are based on the physical interaction with the environment. As a result, the number of “clusters” found using ray tracing is significantly larger than those based on the clustering algorithm. Therefore, the multipath component distance (MCD) metric [26] is used to group rays that are close to each other in the spatio-temporal domain. The MCD is calculated for a combination of two different reflections, i and j , as

$$\text{MCD}_{ij} = \sqrt{\|\text{MCD}_{\text{DOD},ij}\|^2 + \|\text{MCD}_{\text{DOA},ij}\|^2 + \text{MCD}_{\tau,ij}^2}$$

where the delay distance is given by

$$\text{MCD}_{\tau,ij} = \xi \frac{|\tau_i - \tau_j|}{\Delta\tau_{\max}} \frac{\tau_{std}}{\Delta\tau_{\max}}. \quad (8)$$

Here, $\Delta\tau_{\max} = \max_{i,j} \{|\tau_i - \tau_j|\}$, and τ_{std} is the standard deviation of the delays. For our purposes, $\xi = 3$ was found to be a suitable delay scaling factor. The MCD for angular data is given by $\text{MCD}_{\text{DOD/DOA},ij} = (1/2)|\mathbf{a}_i - \mathbf{a}_j|$, where

$$\mathbf{a}_i = [\sin(\theta_i) \cos(\phi_i), \sin(\theta_i) \sin(\phi_i), \cos(\theta_i)]^T.$$

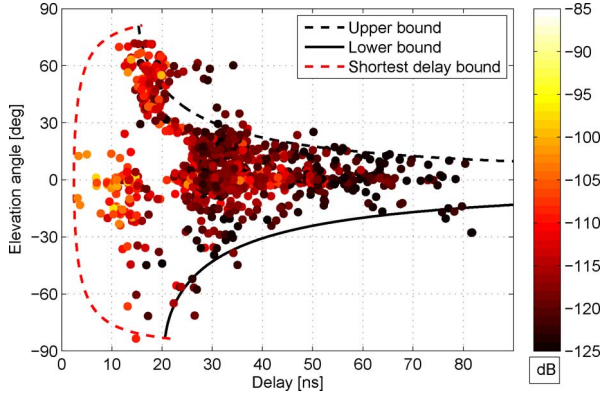


Fig. 7. Elevation-delay dependence model for the stochastic channel model.

Before calculating the MCD, all rays are sorted with respect to their delays. Then, the MCD between the ray with the shortest delay and all other rays are calculated, and all rays with a $MCD < 0.25$ are grouped together with the ray with the shortest delay. Then, the same thing is done again for the remaining rays, until all rays have been assigned to a group. The cluster delays and angles are then determined as the delay and angles of the rays with the shortest delays in each group.

2) *Stochastic Model*: In the stochastic model, the cluster angles are modeled using conditional probabilities. The cluster delays, T_k , are modeled based on exponentially distributed cluster interarrival times. Then, the cluster elevation angles, Θ_k are determined using a joint pdf for the elevation angles conditioned on the cluster delay, i.e.,

$$f(T_k, \Theta_k) = f(\Theta_k|T_k)f(T_k) \quad (9)$$

where $f(\Theta_k|T_k)$ is the conditional cluster elevation pdf and $f(T_k)$ is the marginal pdf for the cluster delay. This conditional pdf is determined empirically by considering the possible elevation angles for first and second order reflections in a room with certain dimensions. The idea is that this conditional pdf should reflect upon the possible elevation angles for several different scenarios, with the Tx and Rx placed at different height. Here, we note that this paper only includes measured results for a single height of the Tx and Rx arrays. However, for the conditional pdf, we consider hypothetical scenarios where the Tx is located at a table at different heights, h_1 , varying from 5–40 cm above the table, emulating a laptop or a similar device. The Rx is located at heights, h_2 , varying from 5 cm above the table height up to 5 cm from the ceiling, thereby emulating a device such as a DVD-player, projector or internet access point.

Then, three different curves are used to put bounds on the possible elevation angles for the clusters. The first two curves, the upper and lower bounds, are determined by the maximum and minimum elevation angles for the second order reflections as a function of delay. The third bound, the shortest delay bound, is given by the curve for the shortest possible delay at a given elevation angle for a specific Tx-Rx separation, and is thus different for different scenarios. These three curves are shown in Fig. 7, together with the estimated Tx elevation angles of the MPCs as a function of delay.

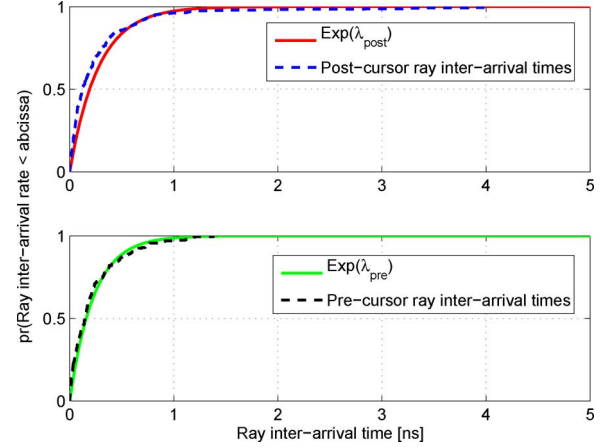


Fig. 8. CDF of the ray interarrival times for the pre- and post-cursor rays in the LOS scenario, and exponential distributions with MLEs of the parameters λ_{pre} and λ_{post} .

Based on the measured data and ray tracing simulations, approximately 40% of the clusters are located within $\pm 5^\circ$ of the horizontal plane. Therefore, we assign a 40% probability for the clusters to be located in the horizontal plane and a 60% probability of being located within the area bounded by the dashed curves in Fig. 7. The clusters that are not assigned to the horizontal plane are randomly placed at a certain elevation angle using a uniform distribution over the supported elevation angles for the given delay, i.e.,

$$f(\Theta_l|T_l) = \frac{1}{\Theta_{\max}(T_l) - \Theta_{\min}(T_l)}. \quad (10)$$

The values $\Theta_{\min}(T_l)$ and $\Theta_{\max}(T_l)$ are the smallest and largest possible elevation angles at a given delay, respectively. The azimuth cluster angles are, for simplicity, modeled using a uniform distribution over the interval $[0, 2\pi)$.

D. Intracuster Parameters

Our clustering results confirm that the clusters generally consist of a main peak surrounded by weaker components with longer and shorter delays. Hence, we adopt the same basic intracuster delay model as in [6], where each cluster consists of a number of pre- and post-cursor rays. The ray interarrival times were calculated by taking the delay of each pre- and post-cursor ray and subtracting it with the previous one, thereby creating a set of conditional arrival times.

Fig. 8 shows CDFs for the ray interarrival times for the pre- and post-cursor rays in the LOS scenario and CDFs for exponential distributions with MLEs of the rate parameters λ_{pre} and λ_{post} .

Next, the mean ray decay rates and K-factors for the pre- and post-cursor rays, γ_{pre} , γ_{post} , K_{pre} and K_{post} , were calculated by normalizing each ray with respect to the delay and mean amplitude of each associated cluster and performing a linear regression.

Then, the normalized path amplitude gain distribution of the pre- and post-cursor rays could be calculated by normalizing each ray with respect to the mean ray amplitudes at a certain

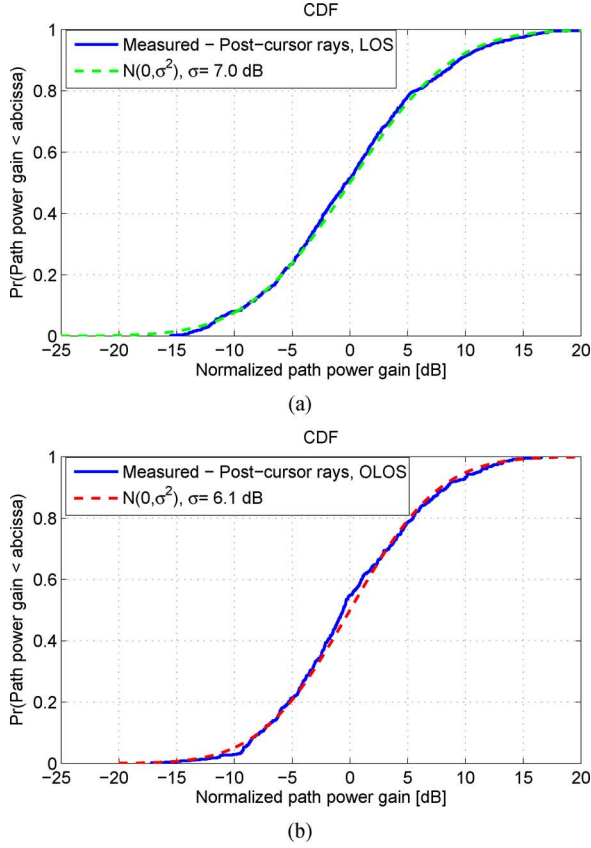


Fig. 9. CDFs of the normalized path power gains of the post-cursor rays and a normal distribution with a MLE of the variance σ^2 , for the (a) LOS and (b) OLOS scenarios.

delay. The power of the pre- and post-cursor rays are appropriately modeled using a log-normal distribution, or a normal distribution in the dB-domain. In Fig. 9, CDFs of the post-cursor ray power distributions for the LOS and OLOS scenarios are shown. The standard deviation of the normal distributions are very similar for both the pre- and post-cursor rays as well as for the LOS and OLOS scenarios, with values in the range of 5.6 to 7.1 dB. These values are similar to the standard deviation for the cluster peak power (i.e., the power of the main ray in each cluster), where the standard deviation is 6.4 dB.

The intracluster angles were calculated by taking the difference of the ray angles and the associated cluster centroid angles. Our results show that a good fit to the measured intercluster angles, $\omega_{k,l}$, is achieved by a zero-mean Laplace distribution with standard deviation σ , with probability density function

$$p(\omega_{k,l}) = \frac{1}{\sqrt{2}\sigma} e^{-|\sqrt{2}\omega_{k,l}/\sigma|}. \quad (11)$$

Fig. 10 shows the CDF of the intracluster azimuth angles of arrival in the LOS scenario, and a Laplacian distribution. Similar curves were obtained for both the LOS and OLOS scenarios in both the azimuth and elevation domains. We also note that the intracluster angles for the azimuth and elevation domains showed very small correlation coefficients, indicating that they can be modeled independently. The estimated values of the variance σ for the azimuth intracluster angles for the DOD and DOA

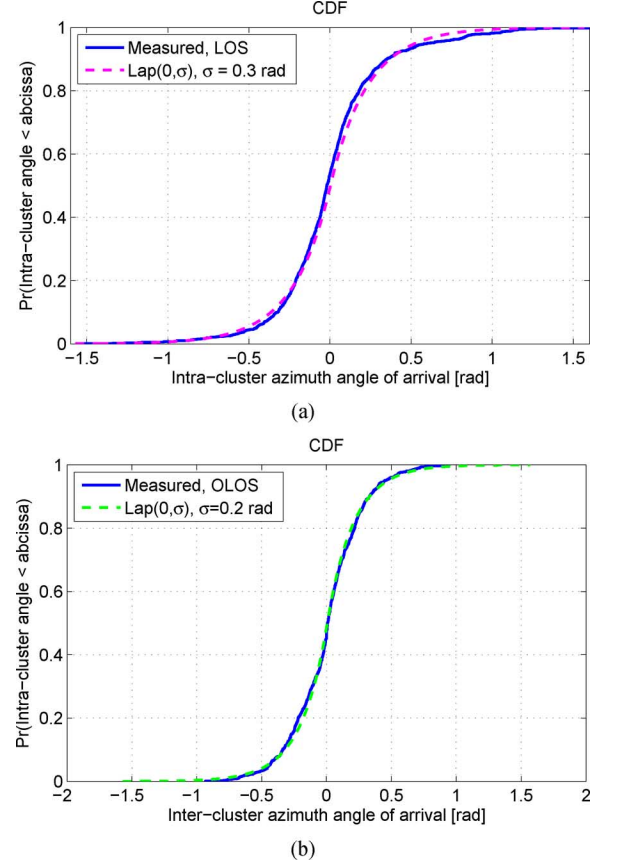


Fig. 10. CDFs of the intracluster azimuth angles of arrival and normal and Laplace distributions with MLEs for the standard deviation σ , for the (a) LOS and (b) OLOS scenarios.

were 0.7 and 0.3 radians, respectively. This difference is most likely attributed to the difference in placement of the Tx and Rx arrays. The Rx array is located close to one of the corners of the room. For the elevation intracluster angles, the values of σ for DOD and DOA were estimated to be 0.2 and 0.3 radians, respectively.

VI. CHANNEL MODEL COMPARISON

In this section, the extracted channel model parameters are compared with those of the IEEE802.11ad and IEEE802.15.3c channel models. Also, the number of clusters and number of rays inside each cluster is also discussed.

A. IEEE 802.11ad Channel Model

In the IEEE802.11ad conference room channel model, the intercluster parameters are largely based on ray tracing results and empirical distributions [6]. For instance, the time and angle of arrival for clusters, as well as attenuation due to reflections, are all modeled using empirical distributions. Hence, it is not possible to compare the intercluster parameters of our proposed model with the IEEE802.11ad model.

However, our proposed model adopts the same basic intracluster model used in [6], making it possible to compare the two models. In Table I, the estimated intracluster time-domain parameters for the LOS and OLOS scenarios are presented

TABLE I
INTRACLUSTER TIME-DOMAIN PARAMETERS; COMPARISON
WITH THE IEEE802.11ad CONFERENCE ROOM MODEL

| Parameter | Notation | LOS | OLOS | 802.11ad |
|------------------|-------------------------|------|------|----------|
| Ray decay time | γ_{pre} [ns] | 4.6 | 4.8 | 3.7 |
| | γ_{post} [ns] | 4.7 | 4.5 | 4.5 |
| Ray K-factor | K_{pre} [dB] | 8.6 | 10.3 | 10 |
| | K_{post} [dB] | 9.0 | 11.0 | 14.2 |
| Ray arrival rate | λ_{pre} [1/ns] | 0.90 | 1.1 | 0.37 |
| | λ_{post} [1/ns] | 0.90 | 1.0 | 0.31 |

TABLE II
INTER- AND INTRACLUSTER TIME-DOMAIN PARAMETERS; COMPARISON
WITH THE IEEE802.15.3c LIBRARY MODEL

| Parameter | Notation | LOS | OLOS | 802.15.3c |
|---------------------------|-----------------------|---------|---------|-----------|
| Cluster arrival rate | Λ [1/ns] | 0.2 | 0.2 | 0.25 |
| Ray arrival rate | λ [1/ns] | 0.9 | 1.0-1.1 | 4.0 |
| Cluster decay rate | Γ [ns] | 8.7 | 8.7 | 12 |
| Ray decay rate | γ [ns] | 4.6-4.7 | 4.5-4.8 | 7.0 |
| Cluster log-normal st. d. | σ_c [dB] | 6.4 | 6.4 | 5.0 |
| Ray log-normal st. d. | σ_r [dB] | 7.0-7.1 | 5.6-6.1 | 6.0 |
| Ray DOD azimuth st. d. | σ_ϕ [deg] | 40 | 23 | 10 |
| Ray DOA azimuth st. d. | σ_ϕ [deg] | 17.2 | 17.3 | N/A |
| Ray DOD elevation st. d. | σ_θ [deg] | 11.4 | 12.1 | N/A |
| Ray DOA elevation st. d. | σ_θ [deg] | 17.2 | 17.5 | N/A |

and compared with the values from the IEEE802.11ad channel model for the conference room environment.

Our results show larger values for the ray arrival rates and somewhat larger ray decay times. These differences might be explained in part by differences in the measurement environment but also due to differences in how the data analysis is performed. Since the rays in our analysis are estimated using a high-resolution algorithm in a real furnished environment, a larger number of rays might be detected, resulting in a different ray arrival rate. The ray K-factors are however similar.

B. IEEE802.15.3c Channel Model

The 802.15.3c channel model uses a Laplacian or Gaussian distribution, with standard deviation σ_ϕ , to model the intra-cluster azimuth angular distribution of the rays inside each cluster. The cluster and ray powers are modeled using log-normal distributions with standard deviations σ_c and σ_r , respectively. This is in agreement with the findings in this paper, and our proposed model also employs a Laplacian distribution for the intracluster angular distribution and log-normal distributions for the cluster and ray powers.

The IEEE802.15.3c channel model supports several different scenarios and channel model parameters have been presented for desktop, office, residential, kiosk and library scenarios [24]. Among these, the library scenario is most similar to the conference room scenario considered in this paper. In Table II, channel model parameters (both inter- and intracluster parameters) for the IEEE802.15.3c library LOS scenario are compared with the parameters of our model.

It can be observed that our results show smaller values for the ray arrival rate compared to the 15.3c model. On the other

hand, our results for the ray arrival rate is also larger compared to that of the IEEE802.11ad model. Furthermore, our results show larger values for the standard deviations of the intracluster angular Laplacian distribution, especially for the DOD in the LOS scenario. The reason for this could be related to differences in how the rays and clusters are identified.

C. Number of Clusters and Rays

In our results, we observed 6–12 and 8–12 clusters in the LOS and OLOS scenarios, respectively, with an average of 10 clusters for both scenarios. The average number of clusters in the 15.3c model is 9, whereas the IEEE802.11ad model has a fixed value of 18 clusters. This difference is due to the fact that the clusters in the IEEE802.11ad model are identified using ray tracing, and several of those clusters would be grouped into one cluster when using a clustering algorithm.

The observed number of rays inside each cluster ranged from 1 up to 38 in one extreme case. The mean observed number of rays in each cluster was 7 for LOS and 9 for OLOS. It was found that the number of rays in each cluster could be modeled using an exponential distribution. However, we have found that due to the ray decay and the large K-factor for the rays, only the first 2–10 rays make a significant contribution to the overall statistics of the simulated channel. Hence, the number of rays in each cluster is set to a fixed number in our model; 6 pre-cursors and 8 post cursor rays for each cluster. The same values are used in the IEEE802.11ad model.

VII. CHANNEL MODEL VALIDATION

In order to assess the performance of the developed channel model, it needs to be validated. In this section, in order to verify the performance of the model, the following metrics are used to compare the outputs from the channel models with the results from the measurements: the relative eigenvalues of the MIMO channel matrices, the RMS delay spread and the direction spread. A large number of MIMO channel matrices were generated using the ray tracing and stochastic models, using the same array geometry, antenna patterns and array positions as in the measurements. For each array position, frequency transfer functions, $\mathbf{H}(f) \in \mathbb{C}^{N_t \times N_r}$, were generated for the same 49×49 MIMO configuration as in the measurement, using a bandwidth of 2 GHz in the frequency range of 61–63 GHz, with 1001 frequency points. This frequency range was chosen since 60 GHz wireless systems typically use bandwidths as large as 2 GHz [2], [3]. Based on these results, we compare the statistical results from the model with the measurements for the three chosen metrics.

A. Eigenvalues

The relative eigenvalues were calculated for a large number of 9×9 MIMO channel matrices. These 9×9 channel matrices are formed using rectangular subarrays based on the larger 49×49 channel matrices at each Tx/Rx array position. We define the n th relative eigenvalue to be

$$\lambda_{n,rel} = \frac{\lambda_n}{\sum_{i=1}^I \lambda_i}. \quad (12)$$

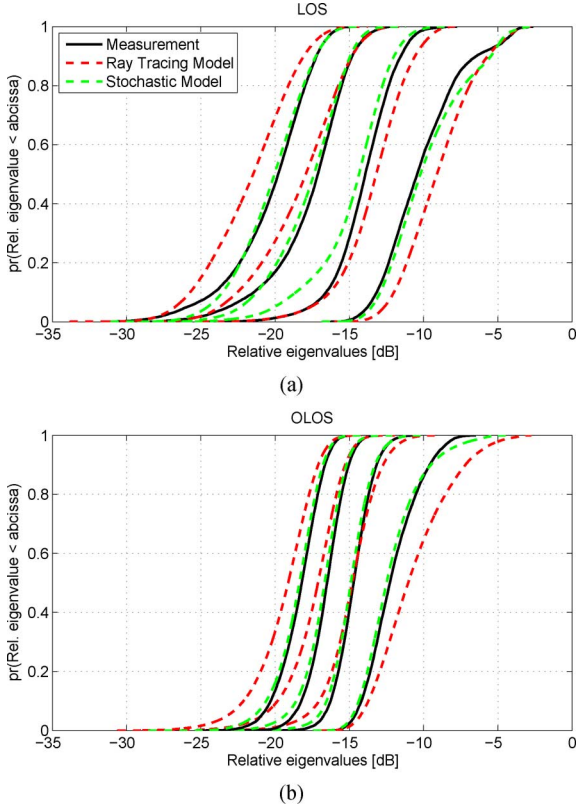


Fig. 11. CDFs of the four strongest relative eigenvalues for the measurement data and for a large number of realizations using the ray tracing and stochastic models in the LOS (a) and OLOS (b) scenarios.

The relative eigenvalues are normalized with respect to the sum of all eigenvalues, which means each relative eigenvalue can be interpreted as a fraction of the total instantaneous channel power. Fig. 11 shows CDFs of the four strongest eigenvalues for the stochastic and ray tracing models as well as the measurements, for both the LOS and OLOS scenarios, using all Tx array positions. Both the stochastic and ray tracing models agree well with the measurement data, with a slightly better agreement for the stochastic model.

B. RMS Delay Spread

The RMS delay spread (RMS DS) was calculated based on the power-delay profiles (PDPs) from the measurements and for the realized PDPs generated by the two models. The PDPs are calculated based on the channel impulse responses (CIRs). Each CIR, $h(\tau)$, is derived by applying a Hann window to $\mathbf{H}(f)$ in order to suppress side lobes, and then taking the inverse Fourier transform. The PDP, $P_h(\tau)$ is then obtained as

$$P_h(\tau) = \frac{1}{N_t N_r} \sum_{n_t=1}^{N_t} \sum_{n_r=1}^{N_r} |h(s_{n_r}, s_{n_t}, \tau)|^2 \quad (13)$$

where s_{n_t} and s_{n_r} denote the spatial position relative to the array origin for the n_t th Tx and n_r th Rx antenna, respectively.

The RMS DS is often calculated by only including values in the PDP that are within a certain range from the peak value. In

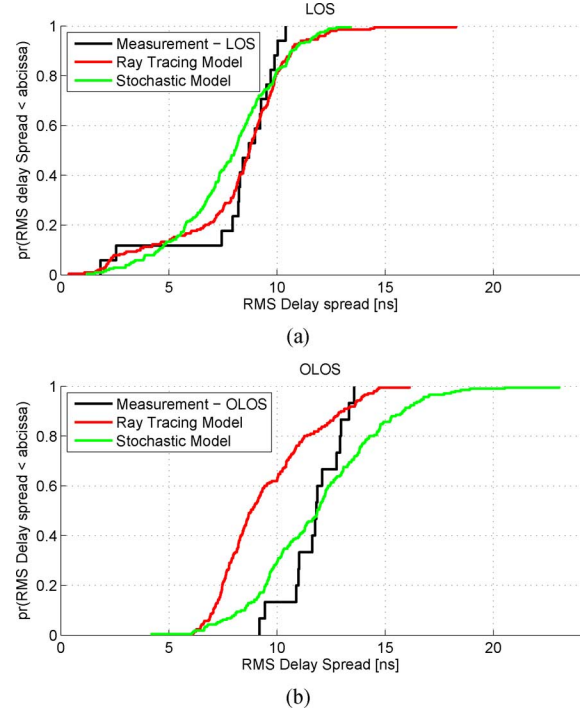


Fig. 12. CDFs of the RMS delay spreads for the measurement data and for a number of realizations using the ray tracing and stochastic models, for the LOS (a) and OLOS (b) scenarios.

this paper, we apply a 30 dB dynamic range when calculating the RMS DS. The RMS DS is then calculated as

$$S_\tau = \sqrt{\frac{\sum_{\tau} P_h(\tau) \tau^2}{\sum_{\tau} P_h(\tau)} - \left(\frac{\sum_{\tau} P_h(\tau) \tau}{\sum_{\tau} P_h(\tau)} \right)^2}. \quad (14)$$

Fig. 12 shows CDFs of the calculated RMS DS for the LOS and OLOS scenarios. It can be noted that both models agree well with the measured RMS DS for the LOS scenario, as seen in Fig. 12(a). For the RMS DS in the OLOS scenarios seen in Fig. 12(b), the ray tracing model seems to underestimate the RMS DS. The reason for this is not known, but might be related to the fact the ray tracing model does not model all the details present in the room and also always places clusters at the same delays and angles for a given Tx-Rx setup.

The stochastic model on the other hand, has a median value that agrees well with the measured values in the OLOS scenario, but exhibits a much larger variation compared to the measured results. Given that only 15 measured values of the RMS DS is available for this comparison, it is difficult to tell whether this variation is reasonable or not. Based on reported values of the RMS DS in the literature for similar scenarios [27], we argue that the values of the RMS DS modeled by the stochastic model is reasonable.

C. Direction Spread

Lastly, the direction spread was chosen as a metric to evaluate and compare the statistical angular properties of the models and the measurements. For this comparison, the MPC estimates from SAGE for the measurements are used in the evaluation.

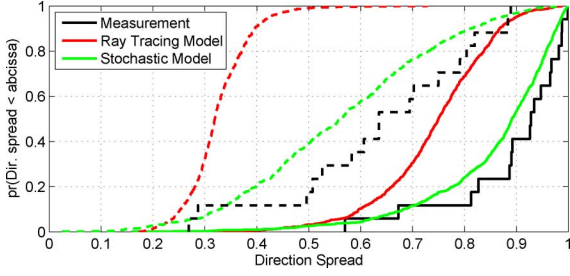


Fig. 13. CDFs of the Tx direction spread in the LOS (dashed curves) and OLOS scenarios (solid curves).

The direction spread, σ_Ω , is calculated for each scenario, using L MPCs, as [28]

$$\sigma_\Omega = \sqrt{\sum_{l=1}^L |\mathbf{e}(\phi_l, \theta_l) - \boldsymbol{\mu}_\Omega|^2 P(\phi_l, \theta_l)} \quad (15)$$

where $P(\phi_l, \theta_l)$ is the normalized power spectrum, whereas ϕ_l and θ_l denote the azimuth and polar angles of the l th MPC, respectively. The mean direction, $\boldsymbol{\mu}_\Omega$, and the unit vector for the direction of the l th MPC, $\mathbf{e}(\phi_l, \theta_l)$, are each given by

$$\boldsymbol{\mu}_\Omega = \sum_{l=1}^L \mathbf{e}(\phi_l, \theta_l) P(\phi_l, \theta_l)$$

$$\mathbf{e}(\phi_l, \theta_l) = [\cos(\phi_l) \sin(\theta_l), \sin(\phi_l) \sin(\theta_l), \cos(\theta_l)]^T. \quad (16)$$

Fig. 13 shows CDFs of the direction spread at the Tx side for the models and measurements. The stochastic model tends to agree quite well with the measurement results, whereas the ray tracing model tends to underestimate the direction spread, especially for LOS scenarios. This is likely explained by the fact that an oversimplified geometry was used in the ray tracing model. In the measurements, there are several strong reflections from objects in the environment such as ceiling lamps and bookshelves [18], and these effects are not taken into account if the room is modeled as rectangular box with tables as the only objects in the ray tracing routine. This shows that it is of importance to include finer details in the environment when using a ray tracing-based approach. As a result, this makes it even more challenging to develop a simple ray tracing-based model that effectively models the statistical behavior of 60 GHz radio channels.

VIII. CONCLUSION

In this paper, we have presented measurement-based results for a 60 GHz double-directional MIMO channel model. The measurements were performed in a conference room using a VNA-based measurement system with 7×7 planar virtual arrays at both the Tx and Rx sides. The measurements included results from 17 LOS and 15 OLOS scenarios. A large number of MPCs were estimated using the SAGE algorithm and then clustered using the K-power-means algorithm. As the antenna patterns were de-embedded in the SAGE algorithm, the proposed channel model supports different antenna types and array geometries.

The intracluster properties describing the rays in each cluster are modeled stochastically. Estimated parameters for the ray decay time, K-factor and arrival rate have been presented. It has also been shown that the intracluster angles are appropriately modeled using a zero-mean Laplacian distribution and that the ray power distribution around the mean can be modeled using a log-normal distribution. Furthermore, we have shown that the angular characteristics of the MPCs and clusters exhibit a clear delay dependence related to overall geometry of the room as well as the objects in the room. Our proposed channel model includes two novel methods of modeling the cluster angular and delay properties; one semi-deterministic model using ray tracing and one stochastic model using joint angular-delay pdfs. Both of these models have been validated against the measurement data using three different metrics; the relative eigenvalues, the RMS delay spread and the direction spread. Both models agree reasonably well with the measured data. We have also provided a detailed comparison of the channel model parameters with those of the IEEE802.11ad and 802.15.3c channel models.

REFERENCES

- [1] R. C. Daniels and R. W. Heath, "60 GHz wireless communications: Emerging requirements and design recommendations," *IEEE Veh. Technol. Mag.*, vol. 2, no. 3, pp. 41–50, Sep. 2007.
- [2] *Part 15.3: Wireless Medium Access Control (MAC) and Physical Layer (PHY) Specifications for High Rate Wireless Personal Area Networks (WPANs), Amendment 2: Millimeter-Wave-based Alternative Physical Layer Extension*, IEEE802.15.3c-2009, Oct. 2009.
- [3] *Part 11: Wireless LAN Medium Access Control (MAC) and Physical Layer (PHY) Specifications Amendment 3: Enhancements for Very High Throughput in the 60 GHz Band*, IEEE802.11ad draft, Dec. 2011.
- [4] C. Gustafson and F. Tufvesson, "Characterization of 60 GHz shadowing by human bodies and simple phantoms," *Radioeng.*, vol. 21, no. 4, Dec. 2012.
- [5] X. An, C. Sum, R. V. Prasad, J. Wang, Z. Lan, J. Wang, R. Hekmat, H. Harada, and I. Niemegeers, "Beam switching support to resolve link-blockage problem in 60 GHz WPANs," in *Proc. IEEE Int. Symp. Personal Indoor and Mobile Radio Comm.*, Sep. 2009, pp. 390–394.
- [6] A. Maltsev, R. Maslennikov, A. Lomayev, A. Sevastyanov, and A. Khorayev, "Statistical channel model for 60 GHz WLAN systems in conference room environment," *Radioeng.*, vol. 20, no. 2, Jun. 2011.
- [7] S. J. Lee and W. Y. Lee, "Capacity of millimetre-wave multiple-input multiple-output channels in a conference room," *IET Commun.*, vol. 6, no. 17, pp. 2879–2885, Nov. 2012.
- [8] M. Park and H. K. Pan, "A spatial diversity technique for IEEE 802.11ad WLAN in 60 GHz band," *IEEE Commun. Lett.*, vol. 16, no. 8, pp. 1260–1262, Aug. 2012.
- [9] X. Zhu, A. Doufexi, and T. Kocak, "Beamforming performance analysis for OFDM based IEEE 802.11ad millimeter-wave WPANs," in *Proc. 8th Int. Workshop Multi-Carrier Syst. Solutions (MC-SS)*, May 3–4, 2011, p. 1.5.
- [10] M. Jacob, S. Priebe, T. Kurner, M. Peter, M. Wisotzki, R. Felbecker, and W. Keusgen, "Extension and validation of the IEEE 802.11ad 60 GHz human blockage model," in *Proc. 7th Eur. Conf. Antennas and Propagation*, Apr. 8–12, 2013, pp. 2806–2810.
- [11] H. Xu, V. Kukshya, and T. S. Rappaport, "Spatial and temporal characteristics of 60-GHz indoor channels," *IEEE J. Sel. Areas Commun.*, vol. 20, no. 3, pp. 620–630, Apr. 2002.
- [12] A. Maltsev *et al.*, "Channel models for 60 GHz WLAN systems," *IEEE 802.11-09/0334r8*, May 2010.
- [13] H. Sawada *et al.*, "Intra-cluster response model and parameter for channel modeling at 60 GHz (Part 3)," *IEEE 802.11-10/0112r1*, Jan. 2010.
- [14] S. Wyne, K. Haneda, S. Ranvier, F. Tufvesson, and A. F. Molisch, "Beamforming effects on measured mm-wave channel characteristics," *IEEE Trans. Wireless Commun.*, vol. 10, no. 11, pp. 3553–3559, 2011.
- [15] S. Ranvier, M. Kyro, K. Haneda, C. Icheln, and P. Vainikainen, "VNA-based wideband 60 GHz MIMO channel sounder with 3D arrays," in *Proc. Radio Wireless Symp.*, San Diego, CA, Jan. 2009, pp. 308–311.

- [16] K. T. Selvan, "A revisit of the reference antenna gain measurement method," in *Proc. 9th Int. Conf. Electromagn. Interference Compatibility*, Feb. 23–24, 2006, pp. 467–469.
- [17] M. Landmann, M. Kaske, and R. S. Thoma, "Impact of incomplete and inaccurate data models on high resolution parameter estimation in multidimensional channel sounding," *IEEE Trans. Antennas Propag.*, vol. 60, no. 2, pp. 557–573, Feb. 2012.
- [18] C. Gustafson, F. Tufvesson, S. Wyne, K. Haneda, and A. F. Molisch, "Directional analysis of measured 60 GHz indoor radio channels using SAGE," presented at the IEEE 73rd Vehicular Technol. Conf. (VTC Spring), Budapest, Hungary, May 2011.
- [19] K. Haneda, C. Gustafson, and S. Wyne, "60 GHz spatial radio transmission: Multiplexing or beamforming?," *IEEE Trans. Antennas Propag.*, vol. 61, no. 11, pp. 5735–5743, Nov. 2013.
- [20] N. Czink, P. Cera, J. Salo, E. Bonek, J.-P. Nuutinen, and J. Ylitalo, "A framework for automatic clustering of parametric MIMO channel data including path powers," in *Proc. IEEE 64th Vehicular Technol. Conf.*, Sep. 25–28, 2006, pp. 1–5.
- [21] D.-J. Kim, Y.-W. Park, and D.-C. D.-J. Park, "A novel validity index for determination of the optimal number of clusters," *IEICE Trans. Inf. Syst.*, vol. E84-D, no. 2, pp. 281–285, 2001.
- [22] Q. H. Spencer, B. D. Jeffs, M. A. Jensen, and A. L. Swindlehurst, "Modeling the statistical time and angle of arrival characteristics of an indoor multipath channel," *IEEE J. Sel. Areas Commun.*, vol. 18, no. 3, pp. 347–360, Mar. 2000.
- [23] C.-C. Chong, C.-M. Tan, D. I. Laurenson, S. McLaughlin, M. A. Beach, and A. R. Nix, "A new statistical wideband spatio-temporal model for 5 GHz band WLAN systems," *IEEE J. Sel. Areas Commun.*, vol. 21, no. 2, Feb. 2003.
- [24] S.-K. Yong *et al.*, TG3c Channel Modeling Sub-Committee Final Report, IEEE Tech. Rep. 15-07-0584-01-003c, 2007.
- [25] C. Gustafson, D. Bolin, and F. Tufvesson, "Modeling the cluster decay in mm-Wave channels," presented at the 8th Eur. Conf. Antennas and Propagation, Hague, Apr. 6–11, 2014.
- [26] N. Czink, P. Cera, J. Salo, E. Bonek, J.-P. Nuutinen, and J. Ylitalo, "Improving clustering performance using multipath component distance," *Electron. Lett.*, vol. 42, no. 1, Jan. 2006.
- [27] S.-K. Yong, P. Xia, and A. Valdes-Garcia, *60 GHz Technology for Gbps WLAN and WPAN: From Theory to Practice*. Hoboken, NJ, USA: Wiley, 2011.
- [28] B. H. Fleury, "First- and second-order characterization of direction dispersion and space selectivity in the radio channel," *IEEE Trans. Inf. Theory*, vol. 46, no. 9, pp. 2027–2044, Sep. 2000.



Carl Gustafson received the M.Sc. degree in electrical engineering from Lund University, Lund, Sweden, where he is currently pursuing the Ph.D. degree at the Department of Electrical and Information Technology.

His main research interests include channel measurements and modeling for 60 GHz and millimeter-wave wireless systems. Other research interests include antenna design, electromagnetic wave propagation, as well as MIMO and UWB systems.



Katsuyuki Haneda (S'03–M'07) received the Doctor of Engineering from the Tokyo Institute of Technology, Tokyo, Japan, in 2007.

Having served as a post-doctoral researcher at the SMARAD Centre of Excellence in the Aalto University (former Helsinki University of Technology) School of Electrical Engineering, Espoo, Finland, he is presently holding an assistant professorship in the Aalto University School of Electrical Engineering. His current research activity focuses on high-frequency radios such as millimeter-wave and beyond,

wireless for medical scenario, radio wave propagation prediction, and in-band full-duplex radio technologies.

Dr. Haneda was the recipient of the best paper award of the antennas and propagation track in the IEEE 77th Vehicular Technology Conference (VTC2013-Spring), Dresden, Germany, and the best propagation paper award in the 7th European Conference on Antennas and Propagation (EuCAP2013), Gothenburg, Sweden. He also received the Student Paper Award presented at the 7th International Symposium on Wireless Personal Multimedia Communications (WPMC '04). He has been an associate editor for the IEEE TRANSACTIONS ON ANTENNAS AND PROPAGATION since 2012 and an editor for the Antenna Systems and Channel Characterization Area of the IEEE TRANSACTIONS ON WIRELESS COMMUNICATIONS since 2013. He also served as a co-chair of the topical working group on indoor environment in the European COST Action IC1004 "Cooperative radio communications for green smart environments" for two years during 2011–2013.



Shurjeel Wyne (S'02–M'08–SM'13) received the Ph.D. degree from Lund University, Lund, Sweden, in March 2009.

Between April 2009 and April 2010, he was a post-doctoral research fellow funded by the High-Speed Wireless Centre at Lund University. Since June 2010, he has held an Assistant Professorship with the Department of Electrical Engineering at COMSATS Institute of Information Technology, Islamabad, Pakistan. His research interests are in the area of wireless communications in particular wireless channel measurements and modeling, 60-GHz Communications, relay networks, and multiple-input multiple-output (MIMO) systems.

Dr. Wyne is a corecipient of the best paper award of the Antennas and Propagation Track in the IEEE 77th Vehicular Technology Conference (VTC2013-Spring), held in Dresden, Germany. He has served as a Technical Program Committee member for various international conferences, including most recently the IEEE International Conference on Communications, (ICC 2013), a flagship conference of the IEEE Communications Society.



Fredrik Tufvesson received the Ph.D. degree in 2000 from Lund University, Lund, Sweden.

After almost two years at a startup company, Fiberless Society, he is now Associate Professor with the Department of Electrical and Information Technology, Lund University. His main research interests are channel measurements and modeling for wireless communication, including channels for both MIMO and UWB systems. Beside this, he also works on distributed antenna systems and radio based positioning.